Revisiting the linear and nonlinear optical properties of nanoparticle-on-mirror–type plasmonic metasurfaces with transformation optics

Yunfei Zhang,[1] Chen Wei,[1] Fuhua Gao,[1] Dangyuan Lei,[2] and Fan Yang[1,*]

[1]*College of Physics, Key Laboratory of High Energy Density Physics and Technology of the Ministry of Education, Sichuan University, Chengdu, Sichuan 610065, China*

[2]*Department of Materials Science and Engineering, City University of Hong Kong, Kowloon 999077, Hong Kong SAR, People's Republic of China*

(Received 20 June 2023; accepted 19 October 2023; published 7 November 2023)

We study the linear optical response and second-harmonic generation from a nanoparticle-on-mirror (NPoM) plasmonic metasurface composed of a nanoparticle array on top of a metal surface. By using transformation optics, the NPoM system is transformed into a simple geometry for the sake of an analytical solution, relaxing the analytical dilemma faced by the NPoM structure. In linear and nonlinear nanophotonics, our analytical method provides a unique understanding of the underlying physical process and endows an efficient scenario in the optical design for the widely used NPoM system.

DOI: 10.1103/PhysRevB.108.205408

I. INTRODUCTION

Nanophotonics mainly explores light-matter interaction at the nanoscale, attracting a wide range of interests in the past few decades [1]. With the development of nanofabrication technology, many kinds of nanoscale structures have been fabricated, such as V shape [2], nanodisk [3,4], bowtie [5], split ring [6], and metallic convex groove [7]. However, these nanostructures usually rely on top-down electron-beam lithography (EBL), a process requiring high precision and limited to a small sample area. In contrast, nanostructures consisting of nanoparticle-on-mirror (NPoM) have obtained considerable attention [8–12] because the NPoM system can be obtained efficiently and simply through bottom-up self-assembly processes while simultaneously not confined by the limited sample area as EBL [13–15]. These advantages of the NPoM-type nanostructure make it widely used for surface-enhanced Raman scattering (SERS) [16–18], enhanced photoluminescence [19–21], fluorescence enhancement [22], hologram [23], data storage [24], and laser [25]. Moreover, the NPoM system can also achieve giant optical nonlinearities, including second-harmonic generation (SHG) [11,26], because it can produce a strong field enhancement while relaxing the constraints of the phase-matching condition [27,28]. Therefore, the NPoM system has become an excellent platform for studying different physical processes and realizing many novel applications.

Despite its rapid development in nanophotonics, the current research on the NPoM system mainly depends on experimental measurements and pure numerical analysis (such as the finite-difference time domain [11], finite-element methods [29], and boundary element method [30]). The analytical solution of the optical response for the NPoM system is still limited. From one perspective, an analytical scenario allows an in-depth look into the underlying physical process, offering a different understanding of the problem. On the other hand, the analytical solution facilitates the optical design of nanophotonic systems, which avoids cumbersome numerical parameter optimizations.

Some semianalytical approaches have been suggested to handle the optical response of the NPoM system. A traditional method to solve the problem is Green's tensor approach with discrete-dipole approximation (DDA), which initially deals with the optical scattering from a nanoparticle in free space [31–33]. Later, the DDA was extended to the case of the NPoM system, where the contribution from the flat surface is incorporated by using Green's function for reflected waves [34–36]. However, the calculation based on DDA can be rather time consuming for large particles or a particle with a high refractive index, leading to an extremely fine mesh in the discretization and a large number of coupled-dipole equations. Another widely used semianalytical method is the quasinormal model (QNM) expansion scenario [37,38]. The optical response from an NPoM system can be expanded as a superposition of many QNM modes [39,40]. The above-mentioned semianalytical methods can be utilized to deal with arbitrary plasmonic systems. However, they still cannot give an explicit analytical formula for the mode profile. Some analytical methods based on Mie theory have been proposed to study the NPoM structure with either particle or substrate is dielectric [41–43], where the traditional multipole expansion approach are extended to incorporate the reflection from the flat surface. However, there is a problem for Mie expansion when both particle and substrate are metallic, where the plasmonic gap mode dominates the optical response.

Fortunately, transformation optics has become an effective tool for studying plasmonic systems [44]. Complex nanostructures can be mapped into simple structures using transformation optics [45], where the analytical solution can be easily obtained. This transformation optics approach has been previously applied to study the linear optical response

*fyang@scu.edu.cn

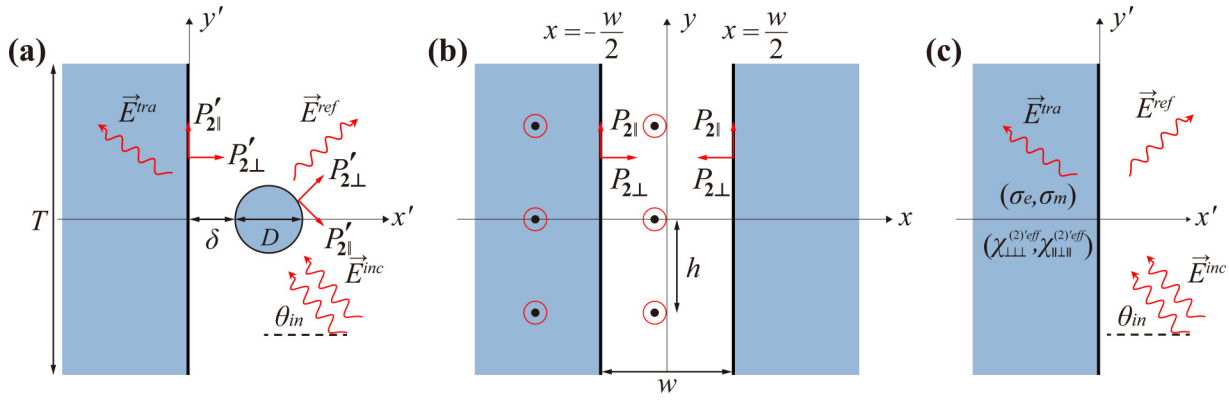

FIG. 1. Geometry, source transformation, and flat surface model. (a) A plane wave impinges on the plasmonic metasurface and creates reflected and transmitted waves in the metasurface frame. (b) Source representation in the MIM frame. (c) A plasmonic metasurface is modeled as a flat metal surface with a pair of surface conductivity (σ_e, σ_m) and nonlinear surface susceptibility $(\chi^{(2)'\text{eff}}_{\perp\perp\perp}, \chi^{(2)'\text{eff}}_{\parallel\perp\parallel})$.

of a single nanoparticle on a flat metal surface [46,47]. In this paper, we further study a nanoparticle array on top of the metal surface, i.e., an NPoM-type metasurface. Our method based on transformation optics treats the whole NPoM as one structure transformed from a simple geometry instead of separating the optical responses from the particle and the substrate as the Mie expansion approach. Both linear and nonlinear (SHG) optical responses are thoroughly explored for the NPoM-type metasurface, providing an analytical solution to this widely used nanostructure.

II. MAPPING OF GEOMETRY AND SOURCE

In this work, we study the two-dimensional case of an NPoM-type plasmonic metasurface composed of a metallic nanoparticle array on top of a metal surface, shown in Fig. 1(a). We set the period as T, the diameter of the nanoparticle as D, and the gap between the nanoparticle and the metal surface as δ. A direct analytical calculation for this NPoM structure is involved because of the complex geometric boundary, so we follow a transformation optics approach. To solve the electromagnetic field analytically, we employ a conformal transformation to map the structure from the metasurface frame in Fig. 1(a) to a metal-insulator-metal (MIM) heterostructure with cavity width w in Fig. 1(b), significantly reducing the complexity of the problem [44]. The metal plane and the nanoparticle interface in the metasurface frame are mapped to two planes of $x = -w/2$ and $w/2$ in the MIM frame, respectively. To distinguish the metasurface and the MIM frame, we use primed coordinates $(z' = x' + iy')$ for the metasurface frame, while the unprimed coordinates $(z = x + iy)$ for the MIM frame. In addition, the primed and unprimed quantity represents a physical quantity in the metasurface and MIM frame. The nanowire array on top of the metal surface in the z' frame can be mapped from a MIM heterostructure in z frame by the conformal mapping [48,49]

$$z' = \frac{T}{2\pi} \ln\left(\frac{1}{ae^{2\pi z/h} - w_0} - y_0\right), \tag{1}$$

where $w_0 = \alpha a e^{-\frac{\pi}{h}w}$, $1 < \alpha < e^{\frac{2\pi}{h}w}$, $y_0 = \frac{\alpha e^{\frac{\pi}{h}w}}{\alpha(1-\alpha^2)}$, and $a = \frac{e^{\frac{\pi}{h}w}}{\alpha^2-1}$. The mapping process consists of a three-step transformation, detailed in the Supplemental Material [50]. These parameter settings make the flat metal surface of the metasurface lie on the y' axis. We point out that the nanoparticle generated by Eq. (1) is not an exact circle but an ellipse. However, this ellipse highly resembles a circle in the case of $D < 0.3T$ (see Supplemental Material for numerical verification [50]).

Throughout this work, the metal is characterized by the Drude model $\varepsilon = 1 - \frac{\omega_p^2}{\omega(\omega+i\gamma)}$, where plasma frequency $\omega_p = 1.36 \times 10^{16}$ rad/s and damping $\gamma = 1 \times 10^{14}$ rad/s (the typical value for the gold). The conformal mapping preserves the permittivity, so the same Drude model characterizes the metallic region of the transformed MIM structure. Note that this conservation of permittivity is only for in-plane components [44], and the out-of-plane component can be safely ignored for the TM polarized pumping.

In the next, we proceed to map the source excitation from the metasurface frame to the MIM frame. A TM-polarized plane wave with a peak intensity of 55 MW/cm^2 (magnetic field in the z direction with amplitude H_0) impinges on the metasurface, resulting in reflected and transmitted waves, respectively. These plane waves in the metasurface frame [see Fig. 1(a)] become two arrays of point sources in the MIM frame with period h [see Fig. 1(b)]. In Fig. 1(b), the incident and the reflected waves are mapped to (x_{s+}, nG) residing in the insulator region, while the transmitted wave is mapped to (x_{s-}, nG) in the metal region on the left. n is an integer, $G = \frac{2\pi}{h}$, $x_{s+} = \frac{h}{2\pi}\ln(w_0/a)$, and $x_{s-} = \frac{h}{2\pi}\ln(\frac{1+w_0y_0}{ay_0})$. The field representation of the point source excitation in the MIM frame can be written as [49]

$$H_z^{\text{ex}} = \begin{cases} \sum_n G\left(a_x(1-r)\frac{e^{-|k_n||x-x_{s+}|}}{|k_n|} - a_y(1+r)\text{sgn}(k_n)\frac{e^{-|k_n||x-x_{s+}|}}{\text{sgn}(x-x_{s+})|k_n|}\right)e^{ik_ny}, & x < |w|/2 \\ \sum_n G\left(-t\frac{k'_{0x}}{k_{0x}}a_x\frac{e^{-|k_n||x-x_{s-}|}}{|k_n|} + ta_y\text{sgn}(k_n)\frac{e^{-|k_n||x-x_{s-}|}}{\text{sgn}(x-x_{s-})|k_n|}\right)e^{ik_ny}, & x < -w/2 \end{cases} \tag{2}$$

where $k_n = nG$, $a_x = -i\frac{k_{0x}T}{4\pi}H_0$, and $a_y = \frac{k_{0y}T}{4\pi}H_0$. r and t are reflection and transmission coefficients for the NPoM metasurface, respectively. The wave vector $k_{0y} = k_0 \sin\theta_{\text{in}}$, $k_{0x} = k_0 \cos\theta_{\text{in}}$, and $k'_{0x} = \sqrt{\varepsilon k_0^2 - k_{0y}^2}$ with θ_{in} being the incident angle. The source representation in Eq. (2) has two kinds of mode, a_x mode and a_y mode. The physical meaning of a_x mode is that the wave vector polarizes parallel to the x direction, while the wave vector of a_y mode is parallel to the y direction. The above point source excites the eigenmode in the MIM frame

$$H_z = \begin{cases} \sum_n Gc_{n+}e^{-|n|Gx}e^{\text{in}Gy}, & x > w/2 \\ \sum_n G(b_{n+}e^{-|n|Gx} + b_{n-}e^{|n|Gx})e^{\text{in}Gy}, & -w/2 < x < w/2 \\ \sum_n Gc_{n-}e^{|n|Gx}e^{\text{in}Gy}, & x < -w/2 \end{cases} \tag{3}$$

from which the electric field can be obtained straightforwardly. Then, by matching the boundary condition at two interfaces $x = -w/2$ and $w/2$ in Fig. 1(b), we can obtain the mode coefficients b_n and c_n of the excited field in the MIM frame. The detailed derivation is included in the Supplemental Material [50]. According to the rule of transformation optics, when the field in the MIM frame is obtained, the field in the metasurface frame can be obtained straightforwardly by [44]

$$\begin{pmatrix} E'_x \\ E'_y \\ H'_z \end{pmatrix} = \frac{1}{\det(\Lambda)} \begin{pmatrix} \frac{\partial x'}{\partial x} & \frac{\partial x'}{\partial y} & 0 \\ -\frac{\partial x'}{\partial y} & \frac{\partial x'}{\partial x} & 0 \\ 0 & 0 & \det(\Lambda) \end{pmatrix} \begin{pmatrix} E_x \\ E_y \\ H_z \end{pmatrix}, \tag{4}$$

where Cauchy-Riemann relations have been used and Λ is the Jacobian matrix defined as $\Lambda_{ij} = \frac{\partial x'_{ij}}{\partial x_{ij}}$. This relation means the z-component magnetic field is invariant while the in-plane electric fields are stretched inhomogeneously.

III. EFFECTIVE MEDIUM FOR LINEAR OPTICAL RESPONSE

For the linear optical response in the far field, the NPoM metasurface shown in Fig. 1(a) can be simplified into a flat metal surface with conductivities shown in Fig. 1(c). Regarding the far-field calculation, we utilize transformation optics to obtain the effective surface polarization for the metasurface by averaging the induced bulk polarization in the MIM frame, which can be expressed as [51]

$$\begin{aligned} P'^{\text{eff}}_{\perp} &= \overline{P^{s'}_x} = \frac{1}{T}\iint_{\text{metal}} \left(\frac{\partial x'}{\partial x}P_x + \frac{\partial x'}{\partial y}P_y\right) dx\,dy, \\ P'^{\text{eff}}_{\parallel} &= \overline{P^{s'}_y} = \frac{1}{T}\iint_{\text{metal}} \left(-\frac{\partial x'}{\partial y}P_x + \frac{\partial x'}{\partial x}P_y\right) dx\,dy. \end{aligned} \tag{5}$$

The overline represents the field averaging and superscript "s" for the surface. The NPoM metasurface considered in our paper is subwavelength, making the plasmonic mode distribute in a thin layer. This subwavelength polarization layer can be safely integrated to give an effective surface polarization. Note that in Eq. (5) the integration of polarization is implemented in one period of the metasurface, which is converted to the integration in the MIM frame for simplicity.

It has been well established that the parallel component of the effective surface polarization gives rise to an effective surface current, while the gradient of the normal component of surface polarization contributes to an effective surface magnetic current, which in Fig. 1(c) reads as [52,53]

$$\begin{aligned} J'^{\text{eff}}_{m,z} &= \frac{1}{\varepsilon_0}\mathbf{n} \times \nabla_{\parallel} P'^{\text{eff}}_{\perp}, \\ J'^{\text{eff}}_{e,y} &= \frac{\partial P'^{\text{eff}}_{\parallel}}{\partial t}. \end{aligned} \tag{6}$$

By analyzing the mode symmetry, we conclude that the a_x mode only contributes to the effective electric surface current and the a_y mode to the effective magnetic surface current. Under light illumination, the plasmonic modes are excited, consuming some energy at the metasurface. This energy dissipation can be modeled by a pair of effective surface conductivity (σ_e, σ_m) when the structural period is subwavelength, as shown in Fig. 1(c) [54]. The complex surface conductivity $\sigma_e = \sigma_{er} + i\sigma_{ei}$ and $\sigma_m = \sigma_{mr} + i\sigma_{mi}$ are expressed as follows:

$$\begin{aligned} \sigma_e &= -\frac{J'^{\text{eff}}_{e1,y} + J'^{\text{eff}}_{e2,y}\lambda_1}{(Z_a + Z_m\lambda_1)H_0/2}, \\ \sigma_m &= \frac{J'^{\text{eff}}_{m1,z} + J'^{\text{eff}}_{m2,z}\lambda_2}{(1+\lambda_2)H_0/2}, \end{aligned} \tag{7}$$

where $Z_a = \frac{k_{0x}}{\omega\varepsilon_0}$ and $Z_m = \frac{k'_{0x}}{\omega\varepsilon_0\varepsilon}$. Moreover, $J'^{\text{eff}}_{(e1,e2),y}$ and $J'^{\text{eff}}_{(m1,m2),z}$ are independent of r and t, which are related to currents in Eq. (6) by $J'^{\text{eff}}_{e,y} = J'^{\text{eff}}_{e1,y}(1-r) + J'^{\text{eff}}_{e2,y}t$ and $J'^{\text{eff}}_{m,z} = J'^{\text{eff}}_{m1,z}(1+r) + J'^{\text{eff}}_{m2,z}t$. The dimensionless coefficients $\lambda_{1,2}$ and the detailed derivation of the above expressions are given in Supplemental Material [50]. The real part of the surface conductivities corresponds to the energy dissipation on the metasurface resulting from the excitation of surface plasmon. In contrast, the imaginary part gives rise to a phase shift as required by the Kramers-Kronig relations [55]. Note that $J'^{\text{eff}}_{(e1,e2),y}$ and $J'^{\text{eff}}_{(m1,m2),z}$ are proportional to input field amplitude H_0, so $\sigma_{e,m}$ is independent of input field intensity.

From the above theory, the metasurface can be characterized using effective surface conductivity when studying the linear response. We consider the effective surface conductivity of the simplified metal plate as a function of frequency ω and gap δ, as shown in Fig. 2. The mode evolution with parameter ω and gap δ can be quantitatively described by the dispersion relation, written as

$$\begin{aligned} \omega &= \omega_{\text{sp}}\sqrt{1 - e^{-2\pi|n|\frac{w}{h}}}, \quad \omega < \omega_{\text{sp}} \\ \omega &= \omega_{\text{sp}}\sqrt{1 + e^{-2\pi|n|\frac{w}{h}}}, \quad \omega > \omega_{\text{sp}} \end{aligned} \tag{8}$$

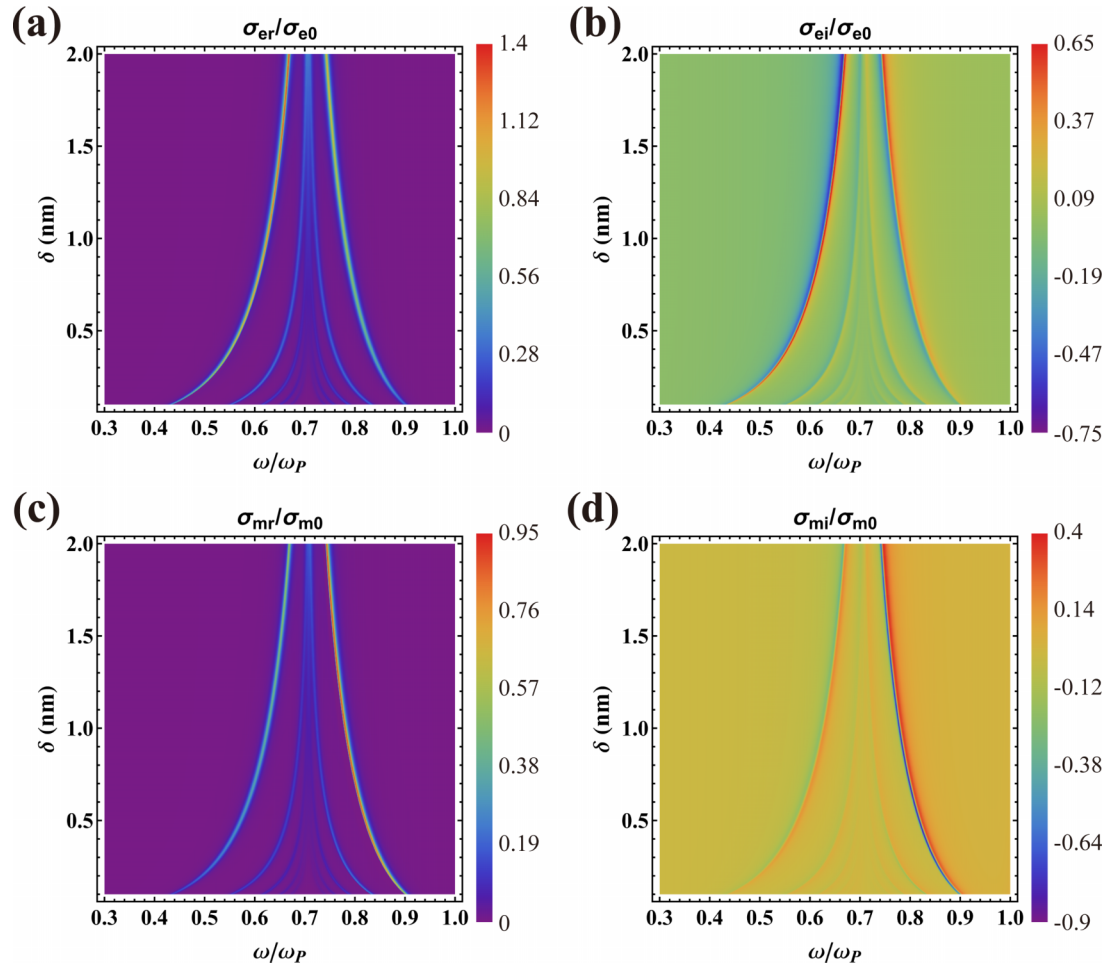

FIG. 2. The effective surface conductivity for the NPoM metasurface. The dependence of the real part (a) and imaginary part (b) of effective electric surface conductivity on frequency and gap for plasmonic metasurface. The dependence of the real part (c) and imaginary part (d) of effective magnetic surface conductivity on frequency and gap for plasmonic metasurface. The parameters setting of the NPoM system are $T = 10$ nm, $D = 2$ nm, and $\theta_{\text{in}} = \pi/4$. The $\sigma_{e0} = Z_0^{-1}$ and $\sigma_{m0} = Z_0$ are the free-space electric and magnetic conductivities, where Z_0 is the impedance of free space.

where n (1,2,...) is the index discretizing the plasmonic mode, and $\omega_{\text{sp}} = \omega_p/\sqrt{2}$ is the surface-plasmon frequency that separates the mode into lower band ($\omega < \omega_{\text{sp}}$) and upper band ($\omega > \omega_{\text{sp}}$). The leftmost and rightmost modes in Fig. 2 correspond to $n = 1$ mode for the lower and upper bands.

The real part of the calculated effective electric surface conductivity is illustrated in Fig. 2(a). The excitation of surface-plasmon-polaritons (SPPs) modes results in resonance for σ_{er}, where the number of resonance peaks increases as the δ decreases. Decreasing the gap makes the NPoM structure more singular, giving broadband and continuous spectrum in the singular limit. This explains why the plasmonic modes distribute into a broader frequency range when decreasing δ. Mathematically, decreasing the gap size δ reduces w/h, decreasing (increasing) the value of ω for the lower (upper) band according to Eq. (8). In the large-gap limit, all the resonance peaks merge into the surface-plasmon frequency ω_{sp}, a signature of the plasmonic resonance of a single nanowire. This is consistent with the analysis of the dispersion relation in Eq. (8), as the δ increases (enlarging w/h), the mode $\omega_n \to \omega_{\text{sp}}$. Figure 2(b) shows the imaginary part of the effective electric surface conductivity, where a sharp phase transition can be observed at the resonance. In Fig. 2(c), the calculated results of the real part of effective magnetic surface conductivity are similar to those of effective electric surface conductivity, except that the stronger resonance appears at the rightmost mode (upper band with mode index 1). The corresponding imaginary part σ_{mi} is shown in Fig. 2(d). Therefore, Fig. 2 summarizes the effective medium for the linear optical response of NPoM-type metasurface, applicable in the inverse design of a metasurface with the desired surface conductivity.

Based on these two effective surface conductivities, we can evaluate the reflection coefficient straightforwardly (see Supplemental Material [50]). We calculate the reflectivity $|r|^2$ and reflection phase change $\phi = \text{Arg}(r)$ as a function of pump frequency ω_1 and gap size δ at $\theta_{\text{in}} = \pi/4$ for metasurface, shown in Figs. 3(a) and 3(b). Since the reflectivity is contributed by electric and magnetic surface conductivities, the reflectivity spectrum has a similar profile as the conductivity spectrum. When the gap gradually decreases, the structure becomes more singular, and the spectrum will change from a few discrete peaks to broadband resonance

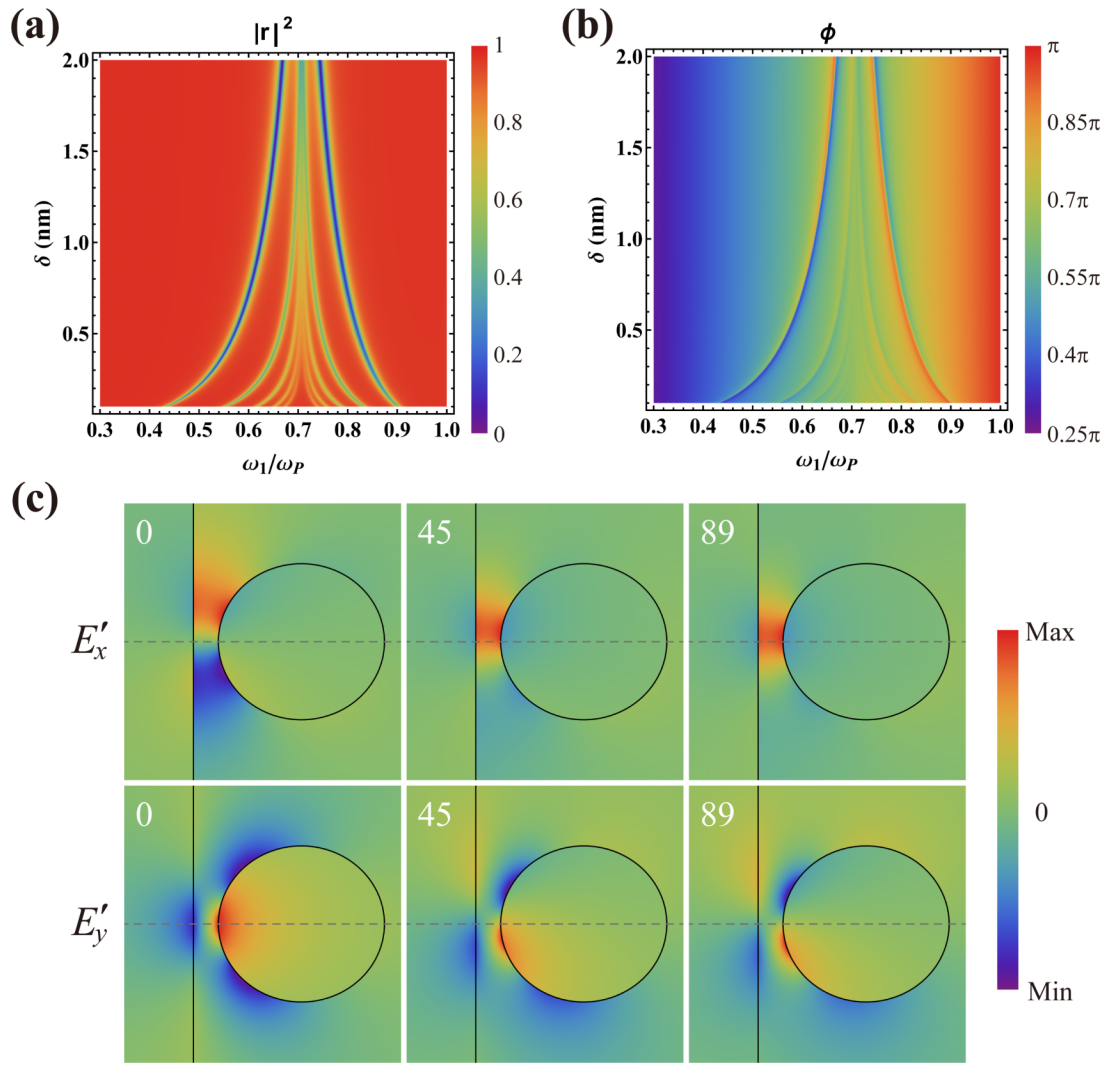

FIG. 3. Linear optical response. (a) Reflectivity $|r|^2$ and (b) phase ϕ of reflection as a function of fundamental frequency ω_1 and gap δ for an NPoM system metasurface. (c) Excited near field at the first resonance peak $\omega_1 = 0.53\omega_p$, where $T = 10$ nm, $D = 2$ nm, and $\delta = 0.3$ nm. The parameters for (a)–(d) are the same as in Fig. 2.

and field enhancement [see Fig. S2(d) in the Supplemental Material [50]]. Moreover, the NPoM metasurface provides a phase shift up to π, efficiently tuning the wavefront in the nanoscale. Furthermore, the variation of incident angle only changes the intensity but not the spectral peak position of the metasurface's effective surface conductivity and reflectivity, as illustrated in Figs. S2(a)–S2(c) of Supplemental Material [50]. This is expected because the field variation does not change the eigenfrequency of the NPoM structure.

Furthermore, we calculate the excited near-field distribution of the first peak at different incident angles, as shown in Fig. 3(c). In the case of normal incidence ($\theta_{\text{in}} = 0^\circ$), the x component E'_x of the excited near field is odd-symmetric mode regarding $y' = 0$, while the y component E'_y has the opposite symmetry. At oblique incidence ($\theta_{\text{in}} = 45^\circ$), the symmetry of the excited field is broken. Near grazing incidence ($\theta_{\text{in}} \approx 90^\circ$), E'_x (E'_y) becomes approximately even- (odd-) symmetric mode. Although the metasurface we study is symmetric, the symmetry of the field concerning the metasurface is broken at the oblique incidence, providing the conditions for SHG.

IV. INDUCED NONLINEAR SURFACE AND BULK POLARIZATION

The above section discusses the linear response of the NPoM metasurface, and next, we turn to its nonlinear optical response. A complete formulation for the nonlinear optical response requires the information of linear optical response. This paper considers the SHG from an NPoM metasurface, one of the most representative nonlinear processes. The second-order nonlinear response cannot arise inside a centrosymmetric medium [56]. For a plasmonic material, the second-order response mainly comes from the surface where the centrosymmetry is broken [57], which is modeled by a nonlinear surface susceptibility. According to the hydrodynamic model, the two second-order nonlinear surface susceptibilities read as [51,58]

$$\chi^{(2)'}_{\perp\perp\perp} = \frac{\varepsilon_0}{4n_0 e}\frac{3\omega_1 + i\gamma}{2\omega_1 + i\gamma}[\varepsilon(\omega_1) - 1]^2,$$
$$\chi^{(2)'}_{\parallel\perp\parallel} = \frac{\varepsilon_0}{2n_0 e}[\varepsilon(\omega_1) - 1]^2, \quad (9)$$

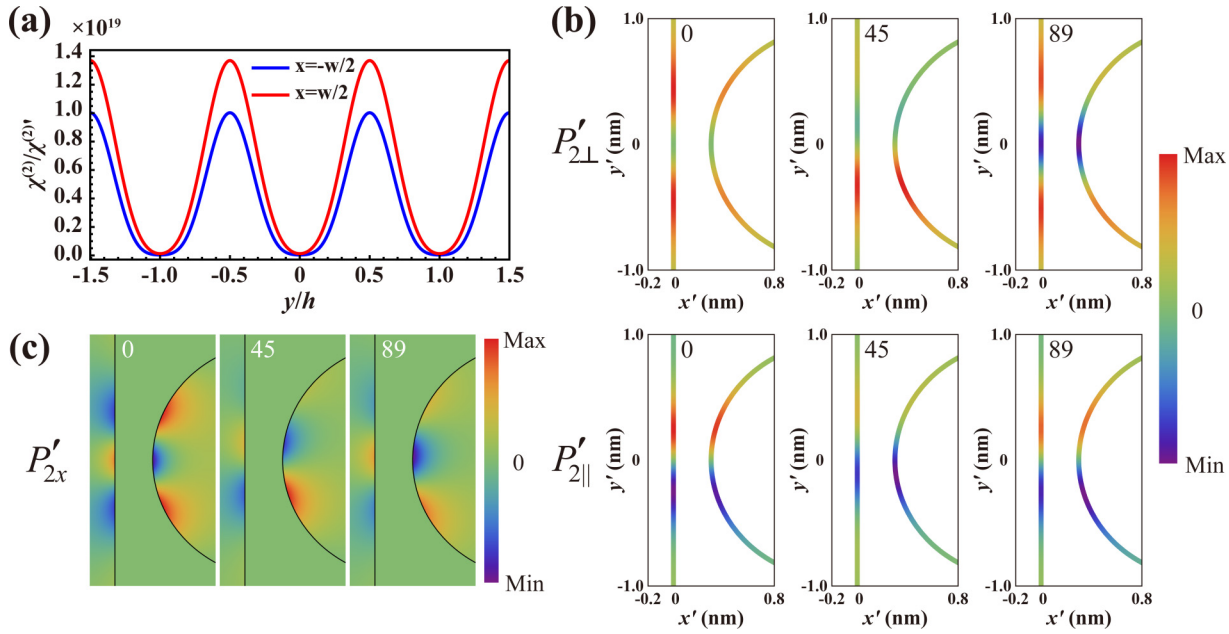

FIG. 4. Nonlinear surface susceptibility and polarization. (a) The nonlinear surface susceptibility in the MIM frame. (b) The normal and parallel components of the nonlinear surface polarization in the metasurface frame. (c) Excited bulk polarization field at the second-harmonic frequency $\omega_2 = 2 \times 0.53\omega_p$. The geometric parameters of the NPoM metasurface are $T = 10$ nm, $D = 2$ nm, and $\delta = 0.3$ nm.

where $n_0 = 5.7 \times 10^{28}$ m^{-3} (a typical value for the gold) is the equilibrium charge density, and $-e$ is the electron charge. Then, the two nonlinear surface polarizations in the metasurface frame can be computed as

$$\begin{aligned} P'_{2\perp}(\omega_2 = \omega_1 + \omega_1) &= \varepsilon_0 \chi^{(2)'}_{\perp\perp\perp} E'_{1\perp} E'_{1\perp}, \\ P'_{2\parallel}(\omega_2 = \omega_1 + \omega_1) &= \varepsilon_0 \chi^{(2)'}_{\parallel\perp\parallel} E'_{1\perp} E'_{1\parallel}, \end{aligned} \tag{10}$$

where $E'_{1\perp}$ and $E'_{1\parallel}$ are the normal and parallel components of the electric field evaluated immediately inside the metal interface at fundamental frequency ω_1, respectively. The direction of $P'_{2\perp}$ and $P'_{2\parallel}$ is defined as shown in Fig. 1(a).

Similar to the linear optical response calculation, the evaluation of the nonlinear optical response from NPoM is converted to the MIM frame [Fig. 1(b)]. According to the transformation rule, the nonlinear surface susceptibility in the MIM frame follows [51,59]:

$$\begin{aligned} \chi^{(2)}_{\perp\perp\perp,\parallel\perp\parallel} &= \left|\frac{dz}{dz'}\right|^2 \chi^{(2)'}_{\perp\perp\perp,\parallel\perp\parallel} \\ &= \left|\frac{h\left(1+\alpha^2-2\alpha\,\mathrm{Cosh}\left[\frac{\pi(w+2z)}{h}\right]\right)}{T(\alpha^2-1)}\right|^2 \chi^{(2)'}_{\perp\perp\perp,\parallel\perp\parallel}. \end{aligned} \tag{11}$$

This mapping preserves the physics of the second-order nonlinear process in Eq. (10), thus allowing us to compute the nonlinear optical response in the simple MIM frame. The nonlinear surface susceptibility in the MIM frame is a periodic function of y with period h as shown in Fig. 4(a), where the blue (red) line shows the variation of the nonlinear surface susceptibility along the interface $x = -w/2$ ($x = w/2$) concerning the y coordinate. With the profile of the nonlinear susceptibility and electric field of linear response in the MIM frame, we can evaluate the nonlinear surface polarization in the virtual space (MIM frame) by

$$\begin{aligned} P_{2\perp}(\omega_2 = \omega_1 + \omega_1) &= \varepsilon_0 \chi^{(2)}_{\perp\perp\perp} E_{1\perp} E_{1\perp}, \\ P_{2\parallel}(\omega_2 = \omega_1 + \omega_1) &= \varepsilon_0 \chi^{(2)}_{\parallel\perp\parallel} E_{1\perp} E_{1\parallel}, \end{aligned} \tag{12}$$

where the physical law of SHG is maintained in the transformed space.

Since the nonlinear surface polarization is conserved under the conformal mapping [51], the $P'_{\perp,\parallel}$ profile in the metasurface frame can be obtained directly by coordinate mapping. In Fig. 4(b), the profile of nonlinear surface polarization for normal (left column), oblique (middle column), and grazing (right column) incidences are illustrated. Under normal incidence, $E'_{1\perp}$ ($E'_{1\parallel}$) possesses an odd (even) symmetry, resulting in an even $P'_{2\perp}$ and an odd $P'_{2\parallel}$. In contrast, $E'_{1\perp}$ ($E'_{1\parallel}$) in the case of glancing incidence possesses an even (odd) symmetry, but the nonlinear polarization gives the same symmetry as that of the normal incidence. In the case of oblique incidence, this symmetry is broken, as illustrated in the middle column of Fig. 4(b).

As a new source excitation, the induced nonlinear surface polarization generates an excited field at the second-harmonic frequency. Fourier series is employed to expand the nonuniform nonlinear surface polarization at the metal-dielectric interface in the MIM frame, formulated as

$$P_{2\perp,2\parallel} = \sum_{n=-\infty}^{\infty} P^n_{2\perp,2\parallel} e^{ik_n y}, \tag{13}$$

where the coefficient can be extracted by

$$P^n_{2\perp,2\parallel} = \frac{1}{h}\int_{-h/2}^{h/2} P_{2\perp,2\parallel} e^{-ik_n y} dy. \tag{14}$$

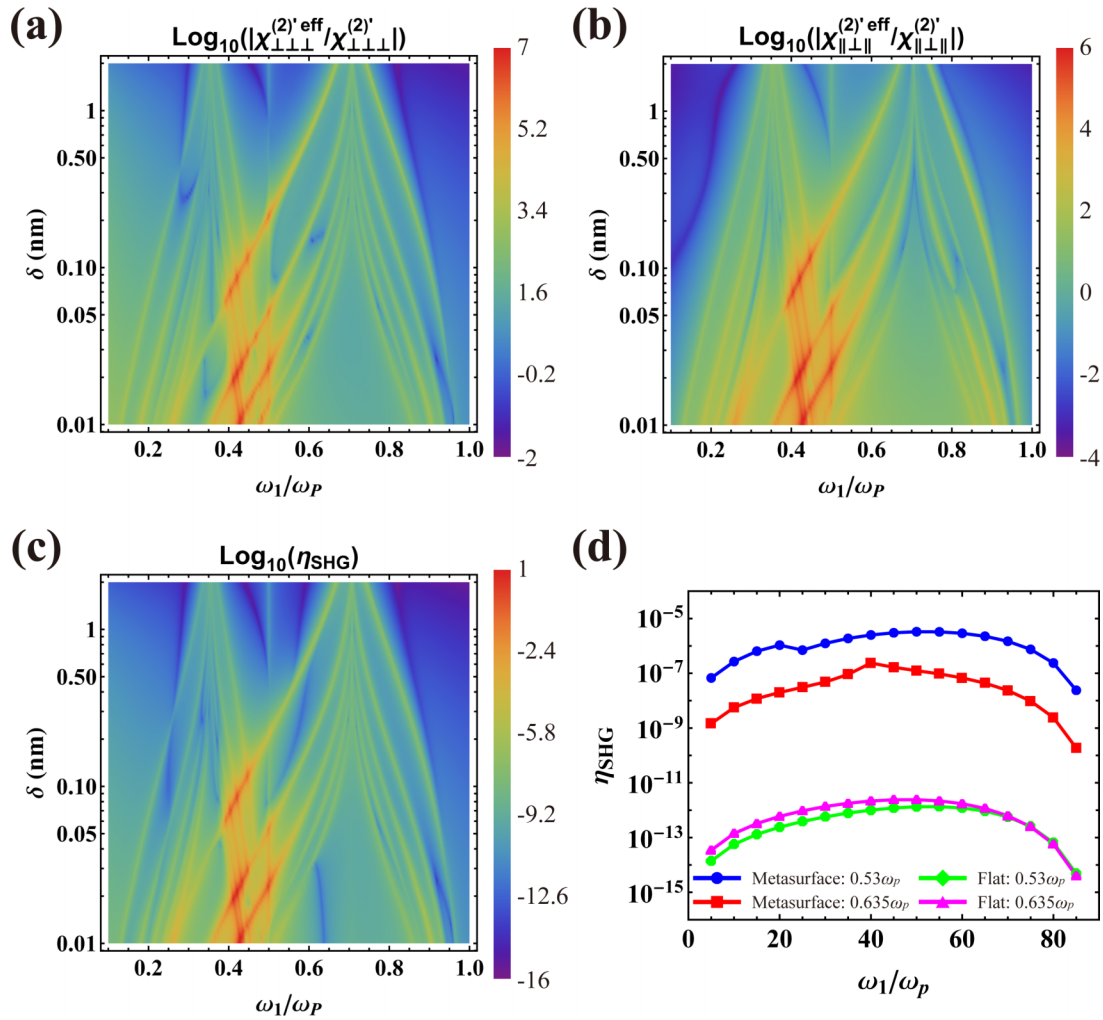

FIG. 5. Effective medium of the NPoM metasurface for the nonlinear far-field response. The dependence of effective nonlinear susceptibility on pump frequency and gap size for (a) $\chi^{(2)'\mathrm{eff}}_{\perp\perp\perp}$ and (b) $\chi^{(2)'\mathrm{eff}}_{\parallel\perp\parallel}$. (c) The dependence of SHG on frequency and gap for singular metasurface. (d) The dependence of SHG on the incident angle for NPoM metasurface and metallic plane, where the parameters are $T = 10$ nm, $D = 2$ nm, and $\delta = 0.3$ nm. The parameters for (a)–(c) are the same as in Fig. 2.

Similarly, the excited field at ω_2 in the MIM frame can also be expanded as $H_{2z} = \sum_n H^n_{2z} e^{ik_n y}$. By matching the tangential fields with boundary conditions at two interfaces $x = -w/2$ and $w/2$, the near field excited by nonlinear surface polarization at ω_2 can be obtained. The specific expression of the excitation field and the detailed derivation procedure are provided in Supplemental Material [50]. The x component of the excited nonlinear near polarization field at $\omega_2 = 2 \times 0.53\omega_p$, P'_{2x}, is shown in Fig. 4(c). At normal and glancing incidence, P'_{2x} is an even-symmetric mode because the nonlinear source excitation has the same symmetry for these two cases. At $\theta_{\mathrm{in}} = \pi/4$, surface polarization's symmetry is broken, resulting in an asymmetric near field.

V. EFFECTIVE MEDIUM FOR NONLINEAR OPTICAL RESPONSE

In the previous section, we have established an effective medium theory for the linear optical response with a pair of effective surface conductivities. This motivates us to further explore the effective medium description for the nonlinear optical response from the NPoM structure. In Fig. 4, the near field and surface polarization at the second-harmonic frequency are illustrated. This near-field profile can be averaged in one period to give a pair of effective surface polarization $(P'^{\mathrm{eff}}_{2\perp}, P'^{\mathrm{eff}}_{2\parallel})$, which is composed by two parts [surface polarization in Fig. 4(b) and bulk polarization in Fig. 4(c)] [51]. The detailed averaging procedure can be found in the Supplemental Material [50]. These two polarizations can be linked with two effective surface nonlinear susceptibilities $\chi^{(2)'\mathrm{eff}}_{\perp\perp\perp,\parallel\perp\parallel}$ shown in Fig. 1(c) by

$$\chi^{(2)'\mathrm{eff}}_{\perp\perp\perp} = \frac{P'^{\mathrm{eff}}_{2\perp}}{\varepsilon_0 E'_{1\perp} E'_{1\perp}} = \frac{\omega_1^2 \varepsilon_0 \varepsilon(\omega_1)^2}{t^2 H_0^2 \left(k^{\omega_1}_{0y}\right)^2} P'^{\mathrm{eff}}_{2\perp},$$

$$\chi^{(2)'\mathrm{eff}}_{\parallel\perp\parallel} = \frac{P'^{\mathrm{eff}}_{2\parallel}}{\varepsilon_0 E'_{1\perp} E'_{1\parallel}} = \frac{\omega_1^2 \varepsilon_0 \varepsilon(\omega_1)^2}{t^2 H_0^2 k^{\omega_1}_{0x} k^{\omega_1}_{0y}} P'^{\mathrm{eff}}_{2\parallel}. \quad (15)$$

In the effective flat surface geometry shown in Fig. 1(c), $E'_{2\perp}$ and $E'_{2\parallel}$ are evaluated at the point immediately inside the metal

region. Note that $P^{\prime\text{eff}}_{2\perp,2\parallel}$ is proportional to the square of pump field magnitude H_0, so the $\chi^{(2)\prime\text{eff}}_{\perp\perp\perp,\parallel\perp\parallel}$ is independent of pump field intensity.

The ratio of the effective susceptibility of NPoM metasurface [Eq. (15)] to the flat metal surface susceptibility [Eq. (9)] for $\perp\perp\perp$ component and $\parallel\perp\parallel$ component are shown in Figs. 5(a) and Fig. 5(b), respectively. The two components of the effective susceptibility have been enhanced by around six or seven orders of magnitude, resulting from the strong field enhancement by plasmonic resonances. Moreover, two branches of modes can be observed, where one originates from plasmonic resonance at ω_1 while the other at ω_2. These two branches of modes can also be characterized by the dispersion relation by Eq. (8), where $\omega = \omega_1$ ($\omega = \omega_2$) for mode at higher (lower) frequency. When increasing the gap size δ, these two branches of modes merge into $\omega_1 = \omega_{\text{sp}}$ and $\omega_2 = \omega_{\text{sp}}$, respectively, degenerating into the spectrum of a single nanowire. Similarly, as the gap decreases, the resonance is redshift for $\omega_1 < \omega_{\text{sp}}$ and $\omega_2 < \omega_{\text{sp}}$, while blueshift for $\omega_1 > \omega_{\text{sp}}$ and $\omega_2 > \omega_{\text{sp}}$. Furthermore, when the gap size shrinks, both branches broaden and overlap to form a double-resonant state near $0.4\omega_p$, further enhancing the effective susceptibilities.

The effective surface polarization ($P^{\prime\text{eff}}_{2\perp}$, $P^{\prime\text{eff}}_{2\parallel}$), as a field excitation, generates second-harmonic fields in the far field. The conversion efficiency of SHG, η_{SHG}, can be solved by applying boundary conditions to the electromagnetic field in Fig. 1(c), which gives

$$\eta_{\text{SHG}} = \left| \frac{\frac{k_{0y}^{\omega_2}(k_{0y}^{\omega_1})^2}{\omega_1^2\varepsilon_0^2\varepsilon(\omega_1)^2\varepsilon(\omega_2)} t^2[4 + 2Z_m(\omega_2)\sigma_e(\omega_2)]\chi^{(2)\prime\text{eff}}_{\perp\perp\perp} - \frac{\omega_2 k_{0x}^{\prime\omega_1} k_{0y}^{\omega_1}}{\omega_1^2\varepsilon_0\varepsilon(\omega_1)^2} t^2[4Z_m(\omega_2) + 2\sigma_m(\omega_2)]\chi^{(2)\prime\text{eff}}_{\parallel\perp\parallel}}{4[Z_a(\omega_2) + Z_m(\omega_2) + Z_a(\omega_2)Z_m(\omega_2)\sigma_e(\omega_2)] + \{4 + [Z_a(\omega_2) + Z_m(\omega_2)]\sigma_e(\omega_2)\}\sigma_m(\omega_2)} \right|^2, \tag{16}$$

where $k_{0y}^{\omega_2} = 2k_{0y}^{\omega_1}$. Note that the transmission coefficient t for linear optical response is only determined by (σ_e, σ_m) at pump frequency ω_1. The detailed derivation of η_{SHG} can be found in the Supplemental Material [50]. In Fig. 5(c), we calculate the SHG efficiency as a function of the frequency ω_1 and gap size δ. As expected, the profile of SHG is similar to that of effective susceptibility, where the large SHG results from the plasmonic mode excitation. In addition, the modes at the pump and second-harmonic frequencies overlap to further enhance the SHG efficiency. Furthermore, a dispersionless mode appears at $\omega_1 = 0.5\omega_p$ or $\omega_2 = \omega_p$, shown in Figs. 5(a)–5(c). The condition for this mode follows $\varepsilon(\omega_2) \to 0$, making the induced surface magnetic current diverge according to Eq. (S28) in the Supplemental Material [50].

In Fig. 5(d), we compare the SHG as a function of the incident angle for the NPoM metasurface and a flat metal surface, where the frequencies of the incident light are $\omega_1 = 0.53\omega_p$ and $0.635\omega_p$, corresponding to the first and second resonance peaks at $\delta = 0.3$ nm in Fig. 3(a), respectively. The results show that the SHG from the metasurface (blue and red lines) is significantly higher than that from the flat metal surface (green and purple lines) in the angular scanning range. The SHG is larger for the oblique incidence than the near-normal and grazing incidence. This is a direct consequence of symmetry breaking, which results in a more efficient SHG. In addition, the validity of our theoretical calculations has been numerically verified by using the COMSOL simulation based on the finite-element method (see Supplemental Material [50]).

VI. FROM TWO DIMENSIONAL TO THREE DIMENSIONAL

All the previous theories in this paper are for the two-dimensional case of an NPoM system. To further check the theory's applicability in analyzing three-dimensional NPoM systems, we simulate the SHG of an NPoM system composed of a gold nanoparticle array on top of a gold surface. Figure 6(a) shows a schematic of the structure of the NPoM system. Figure 6(b) shows the SHG calculated using COMSOL simulations. Similar to the two-dimensional calculation, when shrinking the gap size from 1 to 0.1 nm, the modes near

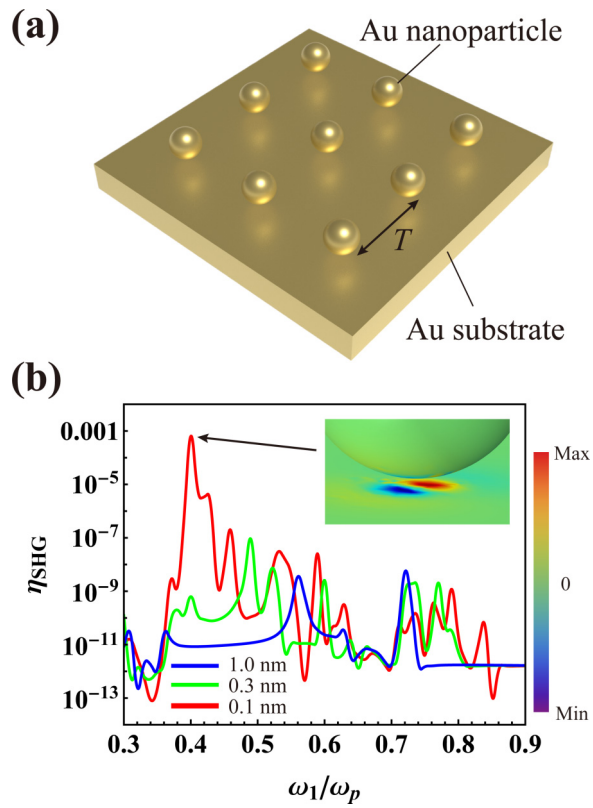

FIG. 6. Numerical calculation of three-dimensional NPoM system. (a) Schematic of the NPoM system composed of gold nanoparticles on top of gold film surface. (b) The SHG of the three-dimensional NPoM system obtained by the finite-element method, where period $T = 10$ nm, diameter $D = 2$ nm, incident angle $\theta_{\text{in}} = \pi/4$, gap $\delta = 0.1$ nm (red line), $\delta = 0.3$ nm (green line), and $\delta = 1.0$ nm (blue line). The inset shows the x component of the nonlinear near field at $\omega_1 = 0.4\omega_p$ for $\delta = 0.1$ nm case.

$\omega_1 = \omega_p/\sqrt{3}$ (plasmonic resonance of a plasmonic nanosphere) and the modes near $\omega_2 = \omega_p/\sqrt{3}$ (equivalently, $\omega_1 = \omega_p/2\sqrt{3}$) get broadened. This makes these two branches of modes eventually overlap and form double-resonant states, resulting in a much higher SHG efficiency near $\omega_1 = 0.4\omega_p$, which is similar to the two-dimensional case shown in Fig. 5(c).

VII. CONCLUSION

In conclusion, we have theoretically investigated the linear and second-order nonlinear responses of an NPoM metasurface. The introduction of transformation optics provides a simple method for obtaining analytical solutions by converting the complex metasurface into a simple MIM structure. Moreover, an effective medium theory has been proposed for the NPoM metasurface, characterized by effective surface conductivity and nonlinear surface susceptibility. These effective parameters can serve as a guideline for the NPoM metasurface design for both linear and nonlinear optics. Furthermore, the plasmonic mode excitation in the NPoM system also enhances the SHG, which can be further enhanced by overlapping the pump and second-harmonic resonance. Finally, despite our analytical framework being established on a periodic NPoM system, it also applies to nonperiodic NPoM structures because the gap mode, rather than the lattice mode, dominates the optical response (numerically demonstrated in the Supplemental Material [50]).

Some future perspectives should be remarked in the end. On the one hand, nonclassical effects [60] due to the quantum nature of electrons have been ignored in our analytical calculation for simplicity. These nonclassical effects, such as nonlocality, electron spillout, and tunneling, have been shown to strongly affect the linear and nonlinear optical response on the mesoscopic scale [61]. These nonclassical effects can be potentially incorporated into our theoretical framework by the semiclassical model [62–64]. On the other hand, our theoretical framework can be further extended to investigate other nonlinear effects, such as Kerr nonlinearity. The Kerr effect modifies the material properties when a high-intense laser beam impinges on the NPoM structure, making it an excellent candidate to explore the time-varying medium and Floquet physics, which mainly focus on the optically induced material dynamics [65–69].

ACKNOWLEDGMENTS

F.Y. acknowledges the financial support from the National Natural Science Foundation of China (Grant No. 12204328), the Fundamental Research Funds for the Central Universities, and the Science Specialty Program (Grant No. 2020SCUNL210) from Sichuan University. D.L. acknowledges the financial support from the Research Grants Council of Hong Kong through a General Research Fund grant (Grant No. 11305521).

[1] Y. Shen, C. S. Friend, Y. Jiang, D. Jakubczyk, J. Swiatkiewicz, and P. N. Prasad, Nanophotonics: Interactions, materials, and applications, J. Phys. Chem. B **104**, 7577 (2000).

[2] R. Czaplicki, A. Kiviniemi, M. J. Huttunen, X. Zang, T. Stolt, I. Vartiainen, J. Butet, M. Kuittinen, O. J. Martin, and M. Kauranen, Less is more: Enhancement of second-harmonic generation from metasurfaces by reduced nanoparticle density, Nano Lett. **18**, 7709 (2018).

[3] L. Zou, W. Withayachumnankul, C. M. Shah, A. Mitchell, M. Bhaskaran, S. Sriram, and C. Fumeaux, Dielectric resonator nanoantennas at visible frequencies, Opt. Express **21**, 1344 (2013).

[4] I. Staude, A. E. Miroshnichenko, M. Decker, N. T. Fofang, S. Liu, E. Gonzales, J. Dominguez, T. S. Luk, D. N. Neshev, I. Brener *et al.*, Tailoring directional scattering through magnetic and electric resonances in subwavelength silicon nanodisks, ACS Nano **7**, 7824 (2013).

[5] S. Kim, J. Jin, Y.-J. Kim, I.-Y. Park, Y. Kim, and S.-W. Kim, High-harmonic generation by resonant plasmon field enhancement, Nature (London) **453**, 757 (2008).

[6] T. Abir, M. Tal, and T. Ellenbogen, Second-harmonic enhancement from a nonlinear plasmonic metasurface coupled to an optical waveguide, Nano Lett. **22**, 2712 (2022).

[7] D. Li, J.-Y. Ou, P. Xie, Z. Liang, W. Wang, W. Wang, H. Zhang, and X. Kuang, Spectroscopic study of gap-surface plasmons in a metallic convex groove array and their applications in nanofocusing and plasmonic sensing, Phys. Rev. B **103**, 245404 (2021).

[8] C. Ciracì, R. Hill, J. Mock, Y. Urzhumov, A. Fernández-Domínguez, S. Maier, J. Pendry, A. Chilkoti, and D. Smith, Probing the ultimate limits of plasmonic enhancement, Science **337**, 1072 (2012).

[9] R. Chikkaraddy, B. De Nijs, F. Benz, S. J. Barrow, O. A. Scherman, E. Rosta, A. Demetriadou, P. Fox, O. Hess, and J. J. Baumberg, Single-molecule strong coupling at room temperature in plasmonic nanocavities, Nature (London) **535**, 127 (2016).

[10] D. Y. Lei, A. I. Fernández-Domínguez, Y. Sonnefraud, K. Appavoo, R. F. Haglund Jr., J. B. Pendry, and S. A. Maier, Revealing plasmonic gap modes in particle-on-film systems using dark-field spectroscopy, ACS Nano **6**, 1380 (2012).

[11] S. Huang, T. Ming, Y. Lin, X. Ling, Q. Ruan, T. Palacios, J. Wang, M. Dresselhaus, and J. Kong, Ultrasmall mode volumes in plasmonic cavities of nanoparticle-on-mirror structures, Small **12**, 5190 (2016).

[12] G.-C. Li, Q. Zhang, S. A. Maier, and D. Lei, Plasmonic particle-on-film nanocavities: A versatile platform for plasmon-enhanced spectroscopy and photochemistry, Nanophotonics **7**, 1865 (2018).

[13] E. Elliott, K. Bedingfield, J. Huang, S. Hu, B. de Nijs, A. Demetriadou, and J. J. Baumberg, Fingerprinting the hidden facets of plasmonic nanocavities, ACS Photonics **9**, 2643 (2022).

[14] T. Ding, D. Sigle, L. Zhang, J. Mertens, B. de Nijs, and J. Baumberg, Controllable tuning plasmonic coupling with nanoscale oxidation, ACS Nano **9**, 6110 (2015).

[15] X. Han, K. Wang, X. Xing, M. Wang, and P. Lu, Rabi splitting in a plasmonic nanocavity coupled to a WS_2 monolayer at room temperature, ACS Photonics **5**, 3970 (2018).

[16] F. Benz, C. Tserkezis, L. O. Herrmann, B. De Nijs, A. Sanders, D. O. Sigle, L. Pukenas, S. D. Evans, J. Aizpurua, and J. J. Baumberg, Nanooptics of molecular-shunted plasmonic nanojunctions, Nano Lett. **15**, 669 (2015).

[17] S. Mubeen, S. Zhang, N. Kim, S. Lee, S. Krämer, H. Xu, and M. Moskovits, Plasmonic properties of gold nanoparticles separated from a gold mirror by an ultrathin oxide, Nano Lett. **12**, 2088 (2012).

[18] R. T. Hill, J. J. Mock, Y. Urzhumov, D. S. Sebba, S. J. Oldenburg, S.-Y. Chen, A. A. Lazarides, A. Chilkoti, and D. R. Smith, Leveraging nanoscale plasmonic modes to achieve reproducible enhancement of light, Nano Lett. **10**, 4150 (2010).

[19] G.-C. Li, Y.-L. Zhang, J. Jiang, Y. Luo, and D. Y. Lei, Metal-substrate-mediated plasmon hybridization in a nanoparticle dimer for photoluminescence line-width shrinking and intensity enhancement, ACS Nano **11**, 3067 (2017).

[20] Y. Wang and T. Ding, Optical tuning of plasmon-enhanced photoluminescence, Nanoscale **11**, 10589 (2019).

[21] C. Lumdee, B. Yun, and P. G. Kik, Gap-plasmon enhanced gold nanoparticle photoluminescence, ACS Photonics **1**, 1224 (2014).

[22] A. Rose, T. B. Hoang, F. McGuire, J. J. Mock, C. Ciracì, D. R. Smith, and M. H. Mikkelsen, Control of radiative processes using tunable plasmonic nanopatch antennas, Nano Lett. **14**, 4797 (2014).

[23] G. Zheng, H. Mühlenbernd, M. Kenney, G. Li, T. Zentgraf, and S. Zhang, Metasurface holograms reaching 80% efficiency, Nat. Nanotechnol. **10**, 308 (2015).

[24] X. Liu, X. Jia, M. Fischer, Z. Huang, and D. R. Smith, Enhanced two-photon photochromism in metasurface perfect absorbers, Nano Lett. **18**, 6181 (2018).

[25] R. F. Oulton, V. J. Sorger, T. Zentgraf, R.-M. Ma, C. Gladden, L. Dai, G. Bartal, and X. Zhang, Plasmon lasers at deep subwavelength scale, Nature (London) **461**, 629 (2009).

[26] G.-C. Li, D. Lei, M. Qiu, W. Jin, S. Lan, and A. V. Zayats, Light-induced symmetry breaking for enhancing second-harmonic generation from an ultrathin plasmonic nanocavity, Nat. Commun. **12**, 4326 (2021).

[27] M. Celebrano, X. Wu, M. Baselli, S. Großmann, P. Biagioni, A. Locatelli, C. De Angelis, G. Cerullo, R. Osellame, B. Hecht *et al.*, Mode matching in multiresonant plasmonic nanoantennas for enhanced second harmonic generation, Nat. Nanotechnol. **10**, 412 (2015).

[28] A. Noor, A. R. Damodaran, I.-H. Lee, S. A. Maier, S.-H. Oh, and C. Ciracì, Mode-matching enhancement of second-harmonic generation with plasmonic nanopatch antennas, ACS Photonics **7**, 3333 (2020).

[29] Y. Huang, L. Ma, J. Li, and Z. Zhang, Nanoparticle-on-mirror cavity modes for huge and/or tunable plasmonic field enhancement, Nanotechnology **28**, 105203 (2017).

[30] X. Zheng, Dedicated boundary element modeling for nanoparticle-on-mirror structures incorporating nonlocal hydrodynamic effects, Adv. Theor. Simul. **5**, 2200480 (2022).

[31] B. T. Draine and P. J. Flatau, Discrete-dipole approximation for scattering calculations, J. Opt. Soc. Am. A **11**, 1491 (1994).

[32] M. A. Yurkin and A. G. Hoekstra, The discrete dipole approximation: An overview and recent developments, J. Quant. Spectrosc. Radiat. Transfer **106**, 558 (2007).

[33] L. Novotny and B. Hecht, *Principles of Nano-optics* (Cambridge University Press, Cambridge, 2012).

[34] M. A. Taubenblatt and T. K. Tran, Calculation of light scattering from particles and structures on a surface by the coupled-dipole method, J. Opt. Soc. Am. A **10**, 912 (1993).

[35] M. Paulus and O. J. Martin, Light propagation and scattering in stratified media: A green's tensor approach, J. Opt. Soc. Am. A **18**, 854 (2001).

[36] A. B. Evlyukhin, C. Reinhardt, E. Evlyukhin, and B. N. Chichkov, Multipole analysis of light scattering by arbitrary-shaped nanoparticles on a plane surface, J. Opt. Soc. Am. B **30**, 2589 (2013).

[37] P. Lalanne, W. Yan, K. Vynck, C. Sauvan, and J.-P. Hugonin, Light interaction with photonic and plasmonic resonances, Laser Photonics Rev. **12**, 1700113 (2018).

[38] W. Yan, R. Faggiani, and P. Lalanne, Rigorous modal analysis of plasmonic nanoresonators, Phys. Rev. B **97**, 205422 (2018).

[39] P. Lalanne, W. Yan, A. Gras, C. Sauvan, J.-P. Hugonin, M. Besbes, G. Demésy, M. Truong, B. Gralak, F. Zolla *et al.*, Quasinormal mode solvers for resonators with dispersive materials, J. Opt. Soc. Am. A **36**, 686 (2019).

[40] C. Gigli, T. Wu, G. Marino, A. Borne, G. Leo, and P. Lalanne, Quasinormal-mode non-hermitian modeling and design in nonlinear nano-optics, ACS Photonics **7**, 1197 (2020).

[41] Yu. V. Vladimirova, V. G. Arakcheev, F. Song, and V. N. Zadkov, Near-field polarization of a high-refractive-index dielectric nanosphere on a dielectric substrate, Phys. Rev. A **100**, 023847 (2019).

[42] H. Zamani, Scattering by a chiral sphere above a half-space, Opt. Express **29**, 31296 (2021).

[43] S. Raza, W. Yan, N. Stenger, M. Wubs, and N. A. Mortensen, Blueshift of the surface plasmon resonance in silver nanoparticles: Substrate effects, Opt. Express **21**, 27344 (2013).

[44] J. B. Pendry, A. Aubry, D. Smith, and S. A. Maier, Transformation optics and subwavelength control of light, Science **337**, 549 (2012).

[45] J. B. Pendry, D. Schurig, and D. R. Smith, Controlling electromagnetic fields, Science **312**, 1780 (2006).

[46] D. Y. Lei, A. Aubry, S. A. Maier, and J. B. Pendry, Broadband nano-focusing of light using kissing nanowires, New J. Phys. **12**, 093030 (2010).

[47] A. Aubry, D. Y. Lei, S. A. Maier, and J. B. Pendry, Plasmonic hybridization between nanowires and a metallic surface: A transformation optics approach, ACS Nano **5**, 3293 (2011).

[48] M. Kraft, Yu. Luo, S. A. Maier, and J. B. Pendry, Designing plasmonic gratings with transformation optics, Phys. Rev. X **5**, 031029 (2015).

[49] F. Yang, E. Galiffi, P. A. Huidobro, and J. B. Pendry, Nonlocal effects in plasmonic metasurfaces with almost touching surfaces, Phys. Rev. B **101**, 075434 (2020).

[50] See Supplemental Material at http://link.aps.org/supplemental/10.1103/PhysRevB.108.205408 for the detailed conformal mapping used to convert an NPoM system into a MIM system; the geometric approximation; the derivation of linear and nonlinear optical response for both near and far field; the validation of the analytical theory with numerical simulation; the extension to nonperiodic NPoM system.

[51] F. Yang and C. Ciracì, Second-harmonic generation from singular metasurfaces, Phys. Rev. B **105**, 235432 (2022).
[52] K. N. Reddy, P. Y. Chen, A. I. Fernández-Domínguez, and Y. Sivan, Revisiting the boundary conditions for second-harmonic generation at metal-dielectric interfaces, J. Opt. Soc. Am. B **34**, 1824 (2017).
[53] M. Albooyeh, Electromagnetic characterization of metasurfaces, Ph.D. thesis, Aalto University, 2015.
[54] F. Yang, P. A. Huidobro, and J. B. Pendry, Transformation optics approach to singular metasurfaces, Phys. Rev. B **98**, 125409 (2018).
[55] J. D. Jackson, *Classical Electrodynamics* (Wiley, New York, 1999).
[56] R. W. Boyd, *Nonlinear Optics* (Academic, New York, 2020).
[57] G. Bachelier, J. Butet, I. Russier-Antoine, C. Jonin, E. Benichou, and P.-F. Brevet, Origin of optical second-harmonic generation in spherical gold nanoparticles: Local surface and nonlocal bulk contributions, Phys. Rev. B **82**, 235403 (2010).
[58] C. Ciracì, E. Poutrina, M. Scalora, and D. R. Smith, Origin of second-harmonic generation enhancement in optical split-ring resonators, Phys. Rev. B **85**, 201403(R) (2012).
[59] F. Yang and C. Cirací, Transformation optics description of direct and cascaded third-harmonic generation, ACS Photonics **10**, 2618 (2023).
[60] M. S. Tame, K. R. McEnery, c. K. Özdemir, J. Lee, S. A. Maier, and M. S. Kim, Quantum plasmonics, Nat. Phys. **9**, 329 (2013).
[61] M. Khalid and C. Ciracì, Enhancing second-harmonic generation with electron spill-out at metallic surfaces, Commun. Phys. **3**, 214 (2020).
[62] R. Esteban, A. G. Borisov, P. Nordlander, and J. Aizpurua, Bridging quantum and classical plasmonics with a quantum-corrected model, Nat. Commun. **3**, 825 (2012).
[63] Yu. Luo, A. I. Fernandez-Dominguez, A. Wiener, S. A. Maier, and J. B. Pendry, Surface plasmons and nonlocality: A simple model, Phys. Rev. Lett. **111**, 093901 (2013).
[64] Y. Yang, D. Zhu, W. Yan, A. Agarwal, M. Zheng, J. D. Joannopoulos, P. Lalanne, T. Christensen, K. K. Berggren, and M. Soljačić, A general theoretical and experimental framework for nanoscale electromagnetism, Nature (London) **576**, 248 (2019).
[65] S. Yin, E. Galiffi, and A. Alù, Floquet metamaterials, eLight **2**, 8 (2022).
[66] A. S. Disa, T. F. Nova, and A. Cavalleri, Engineering crystal structures with light, Nat. Phys. **17**, 1087 (2021).
[67] R. Frank, Coherent control of floquet-mode dressed plasmon polaritons, Phys. Rev. B **85**, 195463 (2012).
[68] R. Frank, Non-equilibrium polaritonics-non-linear effects and optical switching, Ann. Phys. **525**, 66 (2013).
[69] B. Gumhalter and D. Novko, Complementary perturbative and nonperturbative pictures of plasmonically induced electron emission from flat metal surfaces, Prog. Surf. Sci. **98**, 100706 (2023).